

What Determines the Physical Size of a H₂O Megamaser Disk ?

C. Y. Kuo,^{1,2*} F. Gao,³ J. A. Braatz,⁴ D. W. Pesce,^{5,6} E. M. L. Humphreys,^{7,8} M. J. Reid,⁵
C. M. V. Impellizzeri,⁹ C. Henkel,¹⁰ J. Wagner,¹⁰ C. E. Wu,^{1,11}

¹Physics Department, National Sun Yat-Sen University, No. 70, Lien-Hai Rd, Kaosiung City 80424, Taiwan, R.O.C

²Academia Sinica Institute of Astronomy and Astrophysics, P.O. Box 23-141, Taipei 10617, Taiwan, R.O.C.

³Hamburg Observatory, Gojenbergsweg 112, 21029 Hamburg

⁴National Radio Astronomy Observatory, 520 Edgemont Road, Charlottesville, VA 22903, USA

⁵Center for Astrophysics | Harvard & Smithsonian, 60 Garden Street, Cambridge, MA 02138, USA

⁶Black Hole Initiative at Harvard University, 20 Garden Street, Cambridge, MA 02138, USA

⁷Joint ALMA Observatory, Alonso de Cordova 3107, Vitacura, Santiago, Chile

⁸European Southern Observatory (ESO) Vitacura, Alonso de Cordova 3107, Vitacura, Santiago, Chile

⁹Leiden Observatory, Leiden University, PO Box 9513, 2300 RA Leiden, The Netherlands

¹⁰Max-Planck Institut für Radioastronomie, Auf dem Hügel 69, 53121 Bonn, Germany

¹¹Center for Astronomy, National Tsing-Hua University (NTHU), No. 101, Section 2, Kuang-Fu Road, Hsinchu 30013, Taiwan, R.O.C

Accepted XXX. Received YYY; in original form ZZZ

ABSTRACT

High precision mapping of H₂O megamaser emissions from active galaxies have revealed more than a dozen of Keplerian H₂O maser disks that enable a $\sim 4\%$ Hubble constant measurement and provide accurate black hole masses. The maser disks that allow for these important astrophysical applications usually display clear inner and outer edges at sub-parsec scales. It is still unclear what causes these boundaries and how their radii are determined. To understand whether the physical conditions favorable for population inversion of H₂O molecules can determine the inner and outer radii of a maser disk, we examine the distributions of gas density and X-ray heating rate in a warped molecular disk described by power-law surface density profile. With a suitable choice of the disk mass, we find that the outer radius R_{out} of the maser disk predicted from our model can match the observed value, with R_{out} mainly determined by the maximum heating rate or the minimum density for efficient maser action, depending on the combination of the Eddington ratio, black hole mass and disk mass. Our analysis also suggests that the inner edge of a maser disk often lie close to the dust sublimation radius, suggesting that the physical conditions of the dusts may play a role in defining inner boundary of the disk. Finally, our model predicts that H₂O *gigamaser* disks could possibly exist at the center of high-*z* quasars, with disk size of $\gtrsim 10 - 30$ pc.

Key words: keyword1 – keyword2 – keyword3

1 INTRODUCTION

In the nuclear regions of external galaxies hosting active galactic nuclei (AGNs), there exist powerful cosmic masers from the $6_{16} - 5_{23}$ transition of ortho-H₂O molecules at 22.23508 GHz, arising either from a sub-parsec circumnuclear disk (e.g. Kuo et al. 2011; Gao et al. 2016) or from the molecular gas excited by the nuclear wind or jet (e.g. Claussen et al. 1998; Greenhill et al. 2003; Sawada-Satoh et al. 2008; Kuo et al. 2020a; Surcis et al. 2020). These 22 GHz H₂O *megamasers* often display total maser luminosities $\gtrsim 10^6$ greater than typical Galactic maser sources and their extremely high surface brightness allows for maser mapping at sub-milliarcsecond resolution by Very Long Baseline interferometry (VLBI), providing a unique probe of gas distribution and kinematics at sub-parsec scales at the center of a distant galaxy (Lo 2005).

In the prototypical H₂O maser galaxy NGC 4258 (e.g. Herrnstein et al. 1999; Argon et al. 2007; Humphreys et al. 2008), the masing

gas resides in a $\sim 0.13 - 0.26$ pc thin disk viewed almost edge-on and follow Keplerian rotation. These disk properties support black hole (BH) mass measurements to percent-level accuracy (e.g. Kuo et al. 2011; Gao et al. 2017) and provide an accurate geometric distance measurement independent of distance ladders and standard candles (e.g. Reid et al. 2009; Gao et al. 2016; Pesce et al. 2020a).

To identify disk megamasers like NGC 4258 for measuring the Hubble constant H_0 , the Megamaser Cosmology Project (MCP; Reid et al. 2009; Braatz et al. 2010) has made extensive surveys of H₂O megamaser emissions from > 4800 AGNs (Kuo et al. 2018b, 2020b), resulting in the detections of $\gtrsim 30$ candidates of disk masers (Pesce et al. 2015). The follow-up imaging of these candidates has increased the number of H₂O maser disks with high precision VLBI maps by a factor of $\gtrsim 4$ over the past decade. This progress not only enables a 4% H_0 measurement (Pesce et al. 2020b), but also yields accurate BH masses (M_{BH}) for exploring the black hole-host galaxy coevolution (e.g. Kormendy & Ho 2013; Greene et al. 2016). In addition, it provides a new tool for constraining the spins of supermassive BHs (Masini et al. 2022).

* E-mail: cykuo.tara@g-mail.nsysu.edu.tw (NSYSU)

While the progress in the detection and mapping of H₂O maser disks appears to be significant in the past decade, the physics of H₂O maser disks receives little attention and is not well-explored. In particular, it's not yet clear what causes warps seen in every Keplerian maser disks (e.g. Bregman 2009, 2012; Caproni et al. 2007). In addition, it is still uncertain what determines the physical size of a maser disk and confines H₂O megamaser emissions within the narrow range of ~ 0.1 –1 pc in a circumnuclear disk (e.g. Neufeld & Maloney 1995; Gao et al. 2017; Wardle & Yusef-Zadeh 2012). Addressing questions like these is valuable because it would not only improve our understanding of the maser disks themselves, but also allow one to explore unrecognized systematics when using the H₂O megamaser technique for H_0 and BH mass measurement. Moreover, a deeper knowledge of maser disk physics can also allow one to investigate whether hyper luminous H₂O “gigamaser” disks could possibly exist at the high redshift universe (Lo 2005). Investigating this possibility is important because such gigamasers, if exist, would enable the application of the maser technique to high- z galaxies for measuring dynamical BH masses and accurate distances, opening an new avenue to test cosmological models (e.g. King et al. 2014; Lusso et al. 2019) that could solve the *Hubble tension problem* (e.g. Di Valentino et al. 2021).

In this paper, we aim to explore whether the physical conditions favorable for population inversion of H₂O molecules could play the primary role for determining the inner and outer radii of an H₂O maser disk. In section 2, we discuss the measurements of the maser disk radii based on VLBI maps compiled from literature. In Section 3, we make predictions of the inner and outer radii of a maser disk based on the examination of the physical conditions in a circumnuclear disk and compare the predictions with the observed values. The discussion of the high- z H₂O gigamasers is presented in Section 4, and our results are summarized in Section 5.

2 THE PHYSICAL SIZE OF AN H₂O MASER DISK

2.1 The Radius Measurement

The H₂O megamasers in disk configuration (*maser disks* hereafter) often display three distinct spatial and velocity components, including the systemic, redshifted, and blueshifted maser features (Kuo et al. 2011; Pesce et al. 2015). In nearly all cases, the VLBI maps of such maser disks usually show clear inner and outer edges at the sub-parsec scales, defined by the positions of the highest and lowest velocity components of either blueshifted or redshifted masers. When the position of the dynamical center of the disk is available either from disk modeling (e.g. Reid et al. 2013; Kuo et al. 2013, 2015) or rotation curve fitting (e.g. Kuo et al. 2011; Gao et al. 2017), the inner (R_{in}) and outer (R_{out}) radii of a maser disk can be measured *directly* from its VLBI map. Alternatively, if one assumes that maser emissions purely originate from a disk without any components associated with jet or outflow, one could also infer the disk radii *indirectly* from the single-dish spectrum of a maser disk based on the velocities of the high-velocity maser features assuming Keplerian rotation¹ (see details in Gao et al. 2017).

To identify the physical mechanism that determines the size of a H₂O maser disk, we first compile in Table 1 all H₂O megamasers from literature that display geometrically thin maser disks in their VLBI maps (e.g. Kuo et al. 2011; Reid et al. 2013; Gao et al. 2017;

Pesce et al. 2020a). The majority of our sources are drawn from Table 5 in Gao et al. (2017), which provides reliable estimates of disk radii for all “clean”² H₂O maser disks that follow Keplerian rotation. We exclude NGC 4388 listed in Gao et al. (2017) in our analysis because the lack of systemic maser features in this system plus the small number of high-velocity maser components (~ 4) makes it difficult to ascertain whether the maser emissions purely originate from a thin rotating disk. Since the physical mechanism that determines the disk size may not be dependent on the Keplerian nature of a disk, we also include the thin, sub-Keplerian maser disk in NGC 1068 (Greenhill et al. 1996) in our sample for comparison. In total, our sample consists of 16 maser disks. The BH masses and the inner/outer disk radii of these systems are shown in Column (3) through (5) in Table 1.

In the left panel of Figure 1, we plot the BH masses of our maser sample against disk radii in unit of pc. As indicated by the inner and outer edges of each black horizontal line, representing R_{in} and R_{out} for a maser disk, respectively, the maser emissions are mostly confined within the radial range of ~ 0.1 –1 pc for the majority of the sources. The red and blue error bars in the plot show the uncertainties of R_{out} and R_{in} , respectively. Except for the obvious uncertainties in the galaxy distance and maser position measurement, the error bars also include the discrepancy between the disk radii inferred by the direct and indirect methods, which could indicate the systematic uncertainty arising from the limit in the spectral coverage or sensitivity in the VLBI observation. For example, the high sensitivity single-dish spectrum of NGC 1194 (Pesce et al. 2015) suggests that the (weak) redshifted maser feature having the highest velocity appears to lie well outside the spectral coverage of the VLBI observations (Kuo et al. 2011), suggesting that the true inner radius of the disk may be smaller than the value derived from the VLBI map. In addition, the spectra of some sources (e.g. NGC 3393) sometimes reveal faint, isolated maser emissions lying between the the systemic and high-velocity maser complexes in the spectra. Without sensitive VLBI mapping, it's difficult to discern whether these emissions are the systemic masers, the outflow components, or the high-velocity maser features residing close to the outer edge of the maser disk, leading to uncertainties in R_{out} . For more detailed discussion on the error analysis, we refer the readers to Gao et al. (2017).

2.2 The Characteristic Inner Radius of a H₂O maser Disk

As one can see in the left panel of Figure 1, the mean radius of a maser disk appears to increase with the BH mass. This trend was first reported by Wardle & Yusef-Zadeh (2012) based on the data of 8 maser disks, showing that the outer radii can be approximately described by $R_{\text{out}} = 0.3(M_{\text{BH}}/10^7 M_{\odot})$ pc. With the inclusion of 6 more maser disks in their analysis, Gao et al. (2017) obtained a slightly different scaling ($R_{\text{out}} \propto M_{\text{BH}}^{0.57 \pm 0.16}$) and show that both R_{in} and R_{out} are well correlated with the BH mass³, suggesting that M_{BH} plays an important role in determining the inner and outer radii of a maser disk. Because of the significant correlation between R_{out} and M_{BH} , we conjecture that the maser disks may reveal an interesting, characteristic scale if the disk size is expressed in unit of the Schwarzschild radius $R_S = 2GM_{\text{BH}}/c^2$, where G and c are the gravitational constant and the speed of light, respectively.

In the right panel of Figure 1, we plot the inner and outer radii of

¹ The high-velocity maser features refer to the redshifted and blueshifted maser components of a maser disk (Kuo et al. 2011)

² A “clean” maser disk indicates that all maser emissions come from the disk, with no maser components associated with jet or outflow.

³ The Spearman's rank correlation coefficients of 0.71 and 0.62 for R_{in} and R_{out} , respectively (Gao et al. 2017)

Table 1. The Megamaser Sample and the Inner and Outer Radii of the Disks

Galaxy Name	M_{BH} ($10^7 M_{\odot}$)	r_{in} (pc)	r_{out} (pc)	R_{in} ($10^5 R_S$)	R_{out} ($10^5 R_S$)	$R_{\text{out}}/R_{\text{in}}$	μ_{in}	μ_{out}	$\mu_{\text{in}}/\mu_{\text{out}}$	Reference
NGC4258	4.0±0.09	0.11 ^{+0.004} _{-0.004}	0.29 ^{+0.01} _{-0.01}	0.29 ^{+0.01} _{-0.01}	0.76 ^{+0.03} _{-0.03}	2.64	0.121±0.002	0.26±0.005	0.47±0.01	1
NGC2273	0.75±0.05	0.03 ^{+0.01} _{-0.01}	0.08 ^{+0.29} _{-0.01}	0.42 ^{+0.14} _{-0.14}	1.12 ^{+4.05} _{-0.14}	2.67	0.356±0.013	0.337±0.028	1.06±0.10	1
UGC3789	1.04±0.06	0.08 ^{+0.02} _{-0.02}	0.3 ^{+0.19} _{-0.03}	0.81 ^{+0.2} _{-0.2}	3.02 ^{+1.91} _{-0.3}	3.75	0.017±0.005	0.345±0.009	0.05±0.01	1
NGC1194	6.5±0.4	0.54 ^{+0.03} _{-0.25}	1.33 ^{+0.97} _{-0.06}	0.87 ^{+0.05} _{-0.4}	2.14 ^{+1.56} _{-0.1}	2.46	0.075±0.001	0.035±0.001	2.14±0.07	1
NGC3393	3.1±0.37	0.17 ^{+0.02} _{-0.02}	0.6 ^{+0.76} _{-0.04}	0.57 ^{+0.07} _{-0.07}	2.03 ^{+2.57} _{-0.14}	3.53	0.172±0.022	0.047±0.016	3.66±1.33	1
J0437+2456	0.29±0.03	0.06 ^{+0.03} _{-0.03}	0.13 ^{+0.03} _{-0.03}	2.17 ^{+1.08} _{-1.08}	4.69 ^{+1.08} _{-1.08}	2.17	0.208±0.061	0.248±0.093	0.84±0.40	1
NGC2960	1.16±0.07	0.13 ^{+0.04} _{-0.04}	0.37 ^{+0.71} _{-0.04}	1.17 ^{+0.36} _{-0.36}	3.34 ^{+6.41} _{-0.5}	2.85	0.054±0.011	0.043±0.024	1.26±0.75	1
NGC5495	1.05±0.2	0.1 ^{+0.05} _{-0.05}	0.3 ^{+0.05} _{-0.05}	1.0 ^{+0.5} _{-0.5}	2.99 ^{+0.5} _{-0.5}	3.0	—	0.136±0.107	—	1
NGC6323	0.94±0.04	0.13 ^{+0.05} _{-0.05}	0.3 ^{+0.05} _{-0.05}	1.45 ^{+0.56} _{-0.56}	3.34 ^{+0.56} _{-0.56}	2.31	0.108±0.011	0.145±0.023	0.74±0.14	1
ESO558-G009	1.7±0.14	0.2 ^{+0.05} _{-0.05}	0.47 ^{+0.06} _{-0.06}	1.23 ^{+0.31} _{-0.31}	2.89 ^{+0.37} _{-0.37}	2.35	0.055±0.023	0.042±0.042	1.31±1.42	1
NGC5765b	4.55±0.31	0.3 ^{+0.06} _{-0.06}	1.15 ^{+0.07} _{-0.07}	0.69 ^{+0.14} _{-0.14}	2.65 ^{+0.16} _{-0.16}	3.83	0.039±0.002	0.094±0.006	0.41±0.03	1
NGC6264	2.91±0.11	0.24 ^{+0.07} _{-0.07}	0.8 ^{+0.07} _{-0.07}	0.86 ^{+0.25} _{-0.25}	2.88 ^{+0.25} _{-0.25}	3.33	0.182±0.008	0.166±0.023	1.10±0.16	1
UGC6093	2.65±0.23	0.12 ^{+0.07} _{-0.07}	0.24 ^{+0.3} _{-0.08}	0.47 ^{+0.28} _{-0.28}	0.95 ^{+1.18} _{-0.32}	2.0	0.058±0.008	0.038±0.006	1.53±0.32	1
NGC1068	0.8±0.03	0.58 ^{+0.02} _{-0.02}	1.05 ^{+0.02} _{-0.02}	7.59 ^{+0.26} _{-0.26}	13.74 ^{+0.26} _{-0.26}	1.81	—	0.07±0.009	—	2
CGCG074-064	2.42±0.2	0.12 ^{+0.01} _{-0.01}	0.47 ^{+0.04} _{-0.04}	0.53 ^{+0.05} _{-0.05}	2.04 ^{+0.18} _{-0.18}	3.92	0.032±0.001	0.032±0.001	1.00±0.04	3
IC2560	0.44±0.09	0.11 ^{+0.02} _{-0.02}	0.47 ^{+0.03} _{-0.03}	2.62 ^{+0.48} _{-0.48}	11.18 ^{+0.71} _{-0.71}	4.27	0.21±0.003	0.13±0.005	1.62±0.07	1

Note. Column (1) : source name; Column (2): BH mass; Column (3) & (4): the inner and outer radii in unit of pc; Column (5) & (6) : the inner and outer radii in unit of 1×10^5 Schwarzschild radii (R_S); Column(7) : the ratio between R_{out} and R_{in} ; Column(8) & (9) : the obliquity parameters at the inner (μ_{in}) and outer (μ_{out}) edges of a maser disk; Column (10) : the ratio between μ_{in} and μ_{out} ; Column (11) : the reference from which we obtain the BH mass and the disk size : 1. Gao et al. (2017); 2. Greenhill et al. (1996); 3. Pesce et al. (2020a).

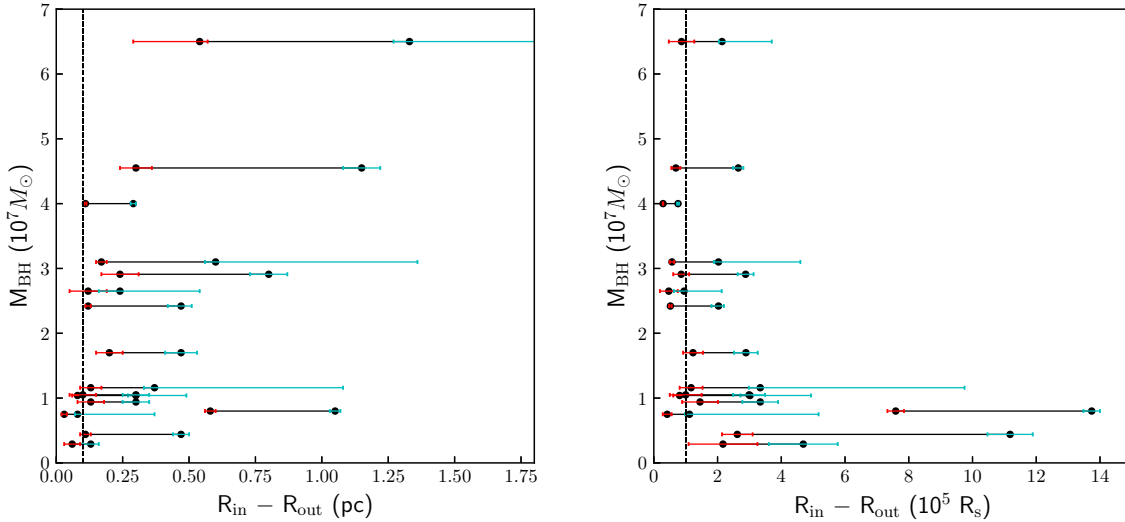


Figure 1. Left panel : The maser disk size in unit of parsec. The edges of each black horizontal bars indicate the inner (R_{in}) and outer (R_{out}) radii of a maser disk, with the red and blue error bars showing the uncertainties in the measurements of R_{in} and R_{out} , respectively. The vertical axis denotes the BH mass for each maser system. The black dashed line in the plot indicates the radius of 0.1 pc; Right panel : the maser disk size in unit of 10^5 Schwarzschild radii (R_S). The majority of the disk megamasers in our sample have inner radii of $R_{\text{in}} \sim 1 \times 10^5 R_S$, indicated by the vertical dashed line.

the maser disks in unit of $10^5 R_S$. As one can see in this plot, while the outer radii show more substantial variation, the majority of our maser disks have inner radii close to $R_{\text{in}} \sim 1 \times 10^5 R_S$ (see the vertical dashed line). The only significant outlier is NGC 1068, whose inner radius is $R_{\text{in}} \sim 7.6 \times 10^5 R_S$. Based on the available proposals that provide tentative explanations for the maser disk size (i.e. Neufeld & Maloney 1995; Wardle & Yusef-Zadeh 2012; Gao et al. 2017), there is no clear reason why the inner radii of most maser disks have

this characteristic scale of $R_{\text{in}} \sim 1 \times 10^5 R_S$. In addition, it is also puzzling why there exist an outlier such as NGC 1068 which shows a significantly larger inner radius than other maser disks. It is likely that the presence of the characteristic inner radius may be associated with the fine-tuning nature of the H_2O megamaser phenomenon while the outlier suggests that some physical parameters in addition to M_{BH} may become important for determining the maser disk size in certain circumstances. As we will show in Section 3.6, the existence of the

characteristic inner radius and the outlier can be understood if the inner edge of a maser disk lies close to the dust sublimation radius of a local Seyfert galaxy, which varies depending on both the mass and the Eddington ratio of an accreting BH.

3 THE MECHANISMS THAT DETERMINE THE SIZE OF A MASER DISK

3.1 The Physical Conditions for Maser Pumping

In the interstellar medium, the $6_{16}-5_{23}$ water maser transition occurs naturally through collisional pumping in a warm molecular cloud if the temperature (T_{H_2}) and the number density (n_{H_2}) of the gas fall within the favored ranges of $400 \lesssim T_{\text{H}_2} \lesssim 1500$ K and $10^7 \lesssim n_{\text{H}_2} \lesssim 10^{11}$ cm $^{-3}$, respectively (e.g. Neufeld et al. 1994; Neufeld 2000; Herrnstein et al. 2005; Lo 2005; Gray et al. 2016). The minimum gas temperature of $T_{\text{min}} \sim 400$ K is required for sufficient collisional pumping given the 6_{16} level lying at $E/k = 643$ K above the ground. Moreover, this temperature threshold is also essential to make a significant enhancement of the water abundance in the cloud ($x_{\text{H}_2\text{O}} \equiv n_{\text{H}_2\text{O}}/n_{\text{H}_2} \gtrsim 10^{-4}$; e.g. Neufeld 2000). Provided that the gas density is below the critical value ($n_{\text{crit}} \lesssim 10^{11}$ cm $^{-3}$) for collisional de-excitation, a sufficiently high density ($n_{\text{H}_2} \gtrsim 10^7$ cm $^{-3}$) is also crucial to make maser pumping efficient.

In addition to the suitable physical conditions of the gas, the presence of cold dusts in the gas cloud is also important for producing the large maser luminosities (Kuo et al. 2018b) observed in water megamasers (Lo 2005). Given that the gas temperature and density fall in the preferred ranges for population inversion, Collison & Watson (1995) demonstrated that the maser emission can be significantly enhanced if there exist cold dust grains in the cloud with a dust temperature $T_{\text{dust}} \sim 50 - 100$ K below the gas temperature. The presence of such cold dusts can absorb nonmasing far-infrared water lines trapped in the cloud, enabling a much larger extent of H $_2$ O molecules maintaining population inversion without being quenched (Collison & Watson 1995; Lo 2005).

To maintain a sufficient temperature for efficient maser pumping, it has been proposed that X-rays from the active nucleus could be the primary heating source for the masing gas (Neufeld et al. 1994; Neufeld & Maloney 1995; Herrnstein et al. 2005). Despite that spiral shock waves travelling a circumnuclear disk (Maoz & McKee 1998) could also provide the energy for maser pumping, the predicted velocity shift of the high-velocity maser features based on this model are shown to be inconsistent with observed drifts seen in the analysis of high-sensitivity spectra of eleven H $_2$ O maser disks (Pesce et al. 2015), making this model less favorable. As a consequence, we will focus in the following discussion on the scenario in which H $_2$ O maser emissions arise in the X-ray dissociation region within a circumnuclear disk subject to X-ray irradiation.

3.2 The Role of X-ray Ionization and Heating

Considering a circumnuclear disk illuminated by the central X-ray source, it is expected that the disk can receive X-heating for maser excitation most efficiently if the disk is warped, allowing one side of the disk plane to be irradiated by X-rays directly. In the well-known picture of maser excitation in NGC 4258 (Neufeld & Maloney 1995, hereafter NM95), it was suggested that the outer edge of the warped maser disk is determined by the critical radius beyond which X-ray ionization becomes strong enough to dissociate all molecules into

atoms. By assuming the viscous gas disk to be in a steady state of accretion, NM95 shows that this critical radius can be expressed as

$$R_{\text{cr}} = 0.040 L_{41}^{-0.426} (\dot{M}_{-5}/\alpha)^{0.898} \mu^{-0.383} M_8^{0.617} \text{ pc}, \quad (1)$$

where $10^{41} L_{41}$ ergs s $^{-1}$ is the 2–10 keV X-ray luminosity of the central source, $10^{-5} \dot{M}_{-5}/\alpha M_{\odot}$ yr $^{-1}$ is the mass accretion rate normalized by the conventional α ($\lesssim 1$) viscosity parameter, and $10^8 M_8$ is the BH mass of the maser system. μ in the above equation is the obliquity parameter defined as $\mu = \cos \eta$, where η is the angle at which the disk is illuminated obliquely with respect to the normal direction of the disk.

To explain the presence of the inner edge in NGC 4258, NM95 observed that the maser disk appears to flatten out close to the inner radius (Miyoshi et al. 1995), suggesting that the obliquity parameter μ falls to zero and the disk is no longer directly illuminated by the X-ray source, making the gas too cold to mase. As a result, they speculated that the inner edge of the maser disk is determined by the nature of the warp. While the NM95 model seems to provide a plausible explanation for the inner and outer edges of NGC 4258 (e.g. Martin 2008), it is not yet well explored whether this model can be applied to H $_2$ O maser disks discovered in the past two decades, whose intrinsic AGN luminosities are 2–3 orders of magnitude higher than that of NGC 4258.

Given the possibility that the H $_2$ O maser disks may not follow steady-state accretion (e.g. Gammie et al. 1999), Gao et al. (2017) proposed a simple alternative model in which the outer edge of a maser disk is determined by the radius beyond which $T_{\text{H}_2} \lesssim 400$ K. Assuming the gas and dust are well-coupled in a maser disk, Gao et al. (2017) uses the dust temperature T_{d} in the optically-thin limit as a proxy of T_{H_2} , finding that the gas temperature is a decreasing function of radius, with the outer radius described by $R_{\text{out}} \propto L_{\text{bol}}^{1/2}$, where L_{bol} is the bolometric AGN luminosity.

While the derived scaling between R_{out} and L_{bol} is broadly consistent with the observations, we find that the simple approximation of R_{out} in Gao et al. (2017) can be further improved by considering the effect of X-ray heating on the gas. It is well-known that the collisions between gas and dust particles do not guarantee $T_{\text{d}} \approx T_{\text{H}_2}$ in a X-ray irradiated gas. The gas and dust can coexist at substantially different temperatures, with the difference varying dependent upon the X-ray heating rate (e.g. Desch et al. 1998; Lo 2005; Namekata & Umemura 2016). In addition, in the region where the gas density is within the favored range for maser pumping, the obscuring column density is required to be large enough (e.g. $N_{\text{H}} \gtrsim 10^{23}$ cm $^{-2}$; Kartje et al. 1999) to avoid molecular dissociation (Neufeld et al. 1994; Neufeld 2000). As shown in Namekata & Umemura (2016), photoheating for dust grains in such a regime is unimportant due to large optical depth. The dust temperature is mainly determined by collisional energy transfer between gas and dust, with $T_{\text{d}} \lesssim 200 - 300$ K, suggesting that using T_{d} in the optically-thin limit to estimate T_{H_2} may lead to non-negligible systematic errors. To obtain a more reliable estimate of R_{out} for a maser disk based on the physical conditions of the interstellar medium, it would be beneficial if one can explore the gas temperature distribution directly with the X-ray heating rate.

3.3 Are disk radii determined by the critical ionization parameter ?

To examine whether the outer edges of the H $_2$ O maser disks in our sample lie at the molecular-to-atomic transition radius R_{cr} as suggested by the NM95 model, we apply Equation 1 to all sixteen maser

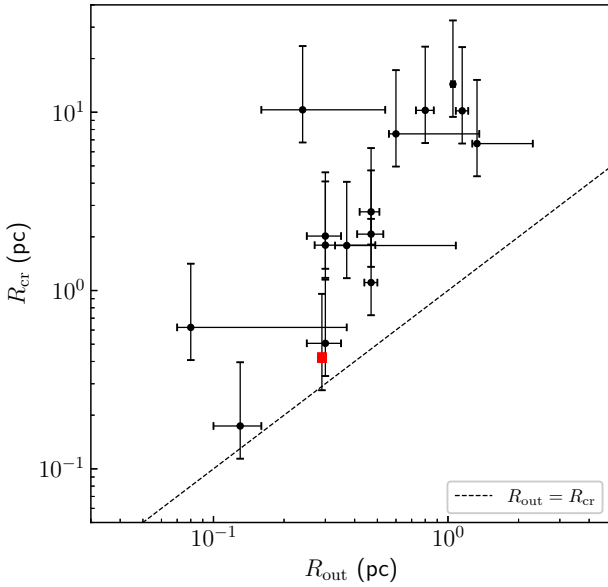


Figure 2. The comparison between the observed outer radius R_{out} of each maser disk and the corresponding critical radius R_{cr} predicted from the NM95 model. The black dashed line indicates the locations where $R_{\text{out}} = R_{\text{cr}}$. Except three sources including NGC 4258 (the filled red square), the majority of the maser disks have R_{cr} substantially greater than R_{out} .

disks listed in Table 1 and compare the predictions with the observed values. When evaluating R_{cr} for our sample, we first estimate the 2-10 keV X-ray luminosity $L_X^{2-10} = 10^{41} L_{41} \text{ ergs s}^{-1}$ by assuming $L_X^{2-10} = 0.1 L_{\text{bol}}$. For all sources except for ESO 558-G009 and CGCG 074-064, we inferred L_{bol} from the reddening corrected [OIII] luminosities $L_{[\text{OIII}]}$ of the maser galaxies (Kuo et al. 2020a). For the two exceptions which do not have $L_{[\text{OIII}]}$ available, we estimate the L_{bol} based on the mid-infrared luminosities derived from SED-fitting (Kuo et al. 2018b), with the bolometric correction given by (Gandhi et al. 2009). Since NM95 assumes a steady-state accretion disk, suggesting that the accretion rate is constant with radius, we calculate the mass accretion rate with $\dot{M} = L_{\text{bol}} / \epsilon c^2$, where ϵ is the accretion efficiency for a Kerr black hole (e.g. Caproni et al. 2007). To obtain the obliquity parameter μ , we performed 3-dimensional bayesian modeling for all maser disks except for NGC 5495 and NGC 1068 using the MCP modeling code described in Reid et al. (2013), Humphreys et al. (2013), Kuo et al. (2015), and Gao et al. (2016). These modelings⁴ give the positions of the dynamical centers of our maser disks and provide the best-fit parameters that characterize the disk warps, enabling us to calculate the obliquity parameter with $\mu = \hat{n} \cdot \hat{r}$, where \hat{n} and \hat{r} are the unit vector of the disk normal and the unit radial vector for a high-velocity maser spot located at a radius r , respectively (Herrnstein et al. 2005). For NGC 5495 and NGC 1068, we simply make a crude estimations of μ based on their maser maps (Gao et al. 2017; Greenhill & Gwinn 1997) because the

⁴ In seven systems listed in Table 1, the maser acceleration measurements required for our modeling are not available. For these cases, we performed modeling by assuming the high-velocity maser features lie within $\leq 15^\circ$ from the mid-line of the disk plane, a typical value expected for maser disks (e.g. Kuo et al. 2011; Gao et al. 2016, 2017).

quality of the VLBI map for NGC 5495 is not good enough for a reliable 3-D modeling whereas NGC 1068 does not follow Keplerian rotation as assumed in our code.

In Columns (8), (9), & (10) in Table 1, we list the obliquity parameters for the inner (μ_{in}) and outer (μ_{out}) edges of each maser disk as well as the ratio $\epsilon\mu = \mu_{\text{in}}/\mu_{\text{out}}$. Based on the values of $\mu_{\text{in}}/\mu_{\text{out}}$, we see no evidence of disk flattening toward the inner edges of all maser disks (i.e. $\mu_{\text{in}}/\mu_{\text{out}} \rightarrow 0$) except for UGC 3789. The ratio is of the order of unity for the majority of the H_2O maser disks, implying that the X-ray heating at the inner edge of the disk would not be significantly less than that at the outer edge. Therefore, the conjecture proposed by NM95 is difficult to account for the presence of the inner edges of most maser disks in our sample.

In Figure 2, we compare the critical radius R_{cr} with the observed R_{out} for each maser disk, with R_{cr} calculated based on the assumption of $\alpha = 0.25$ and $\epsilon = 0.42$ (i.e. the maximum accretion efficiency corresponding to BH spin $a^* = 1$; Caproni et al. 2007). The dashed line shows the locations where $R_{\text{out}} = R_{\text{cr}}$. The error bar in R_{cr} indicates the possible range of the critical radius given the preferred range of $\alpha \sim 0.1 - 0.4$ suggested from observations (e.g. King et al. 2007; Kotko & Lasota 2012). This comparison shows that except for three sources including NGC 4258 (the red filled square in Figure 2), the molecular-to-atomic transition radius is substantially greater than the observed outer radius for the majority of our H_2O maser disks. If one adopts a smaller accretion efficiency (i.e. $\epsilon < 0.42$), R_{cr} would become even greater than R_{out} , suggesting that the NM95 model could not well explain the outer radii of the majority of the maser disks. It is likely that the discrepancy between R_{cr} and R_{out} originates from the deviation from the steady-state assumption in the NM95 model. Alternatively, it is also possible that the outer radius of the maser disk is determined by some other mechanisms, such as the the minimum temperature or density requirements for maser excitation. Both possibilities will be tested with our model presented in the following section.

3.4 The Outer Radius Determined by the Physical Conditions of the Gas

Considering a dusty warm medium where the molecular gas is mainly heated by X-rays, instead of using T_d to approximate T_{H_2} , we use the X-ray heating rate to probe the gas temperature distribution and examine whether the outer radius of a maser disk is determined by the minimum temperature $T_{\text{min}} \sim 400 \text{ K}$ or the maximum X-ray heating rate that breaks molecules into atoms. It is well known that in a medium subject to X-ray heating, one can obtain the gas temperature by balancing the rates of heating and cooling (e.g. emissions from CO and H_2O molecules plus gas-grain collisional cooling; Namekata & Umemura 2016). If one further considers the region within which water maser emissions can occur, assuming a typical value of the water abundance (e.g. $x_{\text{H}_2\text{O}} = n(\text{H}_2\text{O})/n(\text{H}_2) \sim 10^{-4}$), it has been shown by Neufeld (2000) that one can use the equilibrium X-ray heating rate per hydrogen nucleus H_X/n_{H} to replace the gas temperature as the key variable that determines the level populations given the dust temperature T_d and gas density n_{H_2} (Wallin & Watson 1997; Babkovskaia & Poutanen 2004).

In their work, it is demonstrated that the *maximum* heating rate that allows for efficient maser action is $(H_X/n_{\text{H}})_{\text{max}} \sim 1.2 \times 10^{-28} \text{ ergs cm}^3 \text{ s}^{-1}$, beyond which the gas will be subject to molecular dissociation. In addition, the *minimum* heating rate $(H_X/n_{\text{H}})_{\text{min}}$ that ensures $T_{\text{H}_2} \gtrsim 400 \text{ K}$ ranges from $\sim 5.0 \times 10^{-31} \text{ ergs cm}^3 \text{ s}^{-1}$ to $\sim 6.3 \times 10^{-30} \text{ ergs cm}^3 \text{ s}^{-1}$, depending on T_d . If the heating rate of a gas is between $(H_X/n_{\text{H}})_{\text{min}}$ and $(H_X/n_{\text{H}})_{\text{max}}$, it is expected that the

Table 2. Properties of the H₂O Megamaser Systems

Name	$\log L_{\text{bol}}$ (ergs s ⁻¹)	Power-law index	M_{D} ($s = -1.8$)	M_{D} ($s = -1.4$)	M_{D} ($s = -1.0$)	\tilde{M}_{D} ($r \leq 1$ pc)	$\tilde{M}_{\text{D}}/M_{\text{BH}}$ ($r \leq 1$ pc)	$R_{\text{sub, Nenkova}}$ (pc)
NGC4258	41.88	$-2.0 < s \leq -0.8$	0.37	0.12	0.07	0.87	0.0002	0.011±0.003
NGC2273	43.28	$-2.0 < s \leq -0.8$	0.27	0.09	0.05	8.36	0.011	0.055±0.015
UGC3789	44.08	$-2.0 < s \leq -0.6$	5.50	1.83	1.10	12.2	0.012	0.139±0.037
NGC1194	43.44	$-2.0 < s \leq -0.6$	57.3	19.1	11.46	6.48	0.001	0.066±0.018
NGC3393	44.08	$-2.0 < s \leq -0.6$	4.59	1.53	0.92	2.55	0.001	0.139±0.037
J0437+2456	42.54	$-2.0 < s \leq -0.8$	0.34	0.11	0.07	4.07	0.014	0.024±0.006
NGC2960	43.28	$-2.0 < s \leq -0.6$	1.27	0.42	0.25	1.85	0.002	0.055±0.015
NGC5495	42.58	$-2.0 < s \leq -0.8$	0.88	0.29	0.18	1.96	0.002	0.025±0.007
NGC6323	43.94	$-2.0 < s \leq -0.6$	2.86	0.95	0.57	6.36	0.007	0.118±0.032
ESO558-G009	43.19	$-2.0 < s \leq -0.6$	2.42	0.81	0.48	2.19	0.001	0.05±0.013
NGC5765b	44.38	$-2.0 < s \leq -0.6$	33.8	11.3	6.77	5.12	0.001	0.196±0.053
NGC6264	44.84	$-2.0 < s \leq -0.6$	32.0	10.7	6.39	9.98	0.003	0.333±0.09
UGC6093	44.38	$-2.0 < s \leq -0.6$	0.96	0.32	0.19	3.34	0.001	0.196±0.053
NGC1068	45.58	$-2.0 < s \leq -0.5$	69.7	23.2	13.9	12.6	0.016	0.78±0.211
CGCG074-064	43.21	$-2.0 < s \leq -0.6$	2.03	0.68	0.41	1.84	0.001	0.051±0.014
IC2560	43.78	$-2.0 < s \leq -0.6$	5.90	1.97	1.18	5.34	0.012	0.098±0.027

Note. Column (1): source name; Column (2): the AGN bolometric luminosity. Except for ESO558-G009 and CGCG074-064, we adopt L_{bol} from Kuo et al. (2020a), which are estimated from the [OIII] luminosity. For the two exceptions, we estimate their L_{bol} based on the mid-infrared luminosity derived from SED-fitting (Kuo et al. 2018b) with bolometric correction provided by Gandhi et al. (2009); Column (3): the range of the power-law index within which we can find solutions of disk outer radius matching the observed value; Column (4)–(6): the mass of the disk in unit of $10^4 M_{\odot}$ within the outer radius of the maser disk for three representative power-law index $s = -1.8$, $s = -1.4$, and $s = -1.0$, respectively; Column (7): the disk mass in unit of $10^4 M_{\odot}$ within 1 pc of the disk; Column (8): the mass ratio between the disk within 1 pc and the black hole; Column (9): the dust sublimation radius prescribed by Nenkova et al. (2008).

gas temperature would fall within $T_{\text{H}_2} \sim 400 - 1500$ K, the favored range for maser excitation. In addition, T_{H_2} would be an increasing function of $H_{\text{X}}/n_{\text{H}}$ if the dust temperature and water abundance are roughly constant in the region. In the following analysis, we will assume $T_{\text{d}} \sim 300$ K and $x_{\text{H}_2\text{O}} \sim 10^{-4}$ in the masing medium, suggesting $(H_{\text{X}}/n_{\text{H}})_{\text{min}} \sim 3.2 \times 10^{-30}$ ergs cm³ s⁻¹. For the purpose of determining the outer radius of a maser disk, we will simply identify the region within a disk where the X-ray heating rate and gas density fall within the allowed ranges that permit efficient maser action. We will not evaluate the exact gas temperature in the masing region because it will not affect our conclusion.

Following Maloney et al. (1996), we compute the X-ray heating rate per hydrogen nucleus for a gas cloud in the X-ray dissociation region as

$$H_{\text{X}}/n_{\text{H}} = 3.8 \times 10^{-25} \xi_{\text{eff}} \text{ ergs s}^{-1}, \quad (2)$$

where n_{H} is the density of the hydrogen nuclei and ξ_{eff} is the effective ionization parameter defined as

$$\xi_{\text{eff}} = 1.26 \times 10^{-4} \frac{F_{\text{X}}}{n_5 N_{22}^{0.9}}. \quad (3)$$

Here, F_{X} is the *unattenuated* 1 – 100 keV X-ray flux received by a gas clump at a radius r from the central black hole, $n_5 = n_{\text{H}}/10^5$ cm⁻³ and $N_{22} = N_{\text{H}}/10^{22}$ cm⁻² are the normalized total densities of hydrogen nuclei n_{H} and X-ray attenuating column N_{H} for the gas clump, respectively.

To explore the region in the disk where the physical conditions of the gas are suitable for maser excitation, we consider the scenario in which an initially flat, cold molecular disk is warped by a certain mechanism such as *Resonant Relaxation* (e.g. Bregman 2009, 2012), which can warp a sub-parsec scale disk efficiently in a timescale of $\sim 10^7$ years. After the disk get warped, one expects that one side of the warped disk will be subject to direct X-ray illumination which

would deposit thermal energy in the disk. To evaluate the density distribution, we assume that the gas motion is dominated by turbulence (Wallin et al. 1998, 1999), with the turbulence velocity $c_{\text{g}} \sim 2$ km s⁻¹, the typical width of the water maser lines seen in Keplerian maser disks (e.g. Reid et al. 2013; Kuo et al. 2013; Gao et al. 2016). We describe the gas distribution in cylindrical polar coordinates $\vec{r} = (r, \phi, z)$, with the BH sitting at the origin and the mid-plane of the disk lying at $z = 0$. Because of hydrostatic equilibrium, the gas density $\rho(r, z)$ at a radius r from the central black hole and an elevation z above the mid-plane of the geometrically-thin disk can be expressed as

$$\rho(r, z) = \rho_{\text{mid}}(r) \exp\left[-\frac{z^2}{2H^2}\right], \quad (4)$$

where $\rho_{\text{mid}}(r)$ is the gas density at the mid-plane and $H(r)$ is the scale height of the disk, given by $H(r) = c_{\text{g}}(GM_{\text{BH}})^{1/2} r^{3/2}$ (Armitage 2022). The mid-plane density can be calculated with $\rho_{\text{mid}}(r) = \Sigma(r)/[(2\pi)^{1/2}H]$ where $\Sigma(r)$ is the surface density of the disk. Here, we assume that the surface density takes the form of

$$\Sigma(r) = \Sigma_{\text{out}}(r/R_{\text{out}})^s, \quad (5)$$

where the power-law index s is allowed to vary in the interval of $-2 < s < 0$ and Σ_{out} is the surface density at the outer radius of the maser disk (Caproni et al. 2007; Huré et al. 2011; Kuo et al. 2018b). If M_{D} represents the disk mass within R_{out} , one finds that $\Sigma_{\text{out}} = (s+2)M_{\text{D}}/2\pi R_{\text{out}}^2$. If the disk under consideration is in the steady-state accretion, one expects $s = -1.5$ and M_{D} can be expressed as

$$M_{\text{D}} = \frac{4(GM_{\text{BH}})^{1/2} \dot{M} R_{\text{out}}^{1/2}}{3\alpha c_{\text{g}}^2}, \quad (6)$$

where \dot{M} is the mass accretion rate, calculated with $\dot{M} = L_{\text{bol}}/\epsilon c^2$.

Given the above expressions, one can evaluate the number densities of the molecular gas in the disk with

$$n_{\text{H}_2}(r, z) = \rho(r, z) / \zeta_{\text{H}_2} m_{\text{H}}, \quad (7)$$

where $\zeta_{\text{H}_2} = 2.36$ is the mean molecular weight per hydrogen molecule (Fischera & Dopita 2008) and m_{H} is the mass of the hydrogen atom.

Assuming the parcel of gas directly irradiated by the X-ray photons from the $z > 0$ side of the disk is located at the position $\vec{r} = (r, \phi, z)$, we calculate the X-ray absorption column density in between the gas and the X-ray source as

$$N_{\text{H}}(r, z) = \frac{1}{\mu} \int_z^\infty n_{\text{H}}(r, z') dz' = \frac{\Sigma(r)}{\mu \zeta_{\text{H}_2} m_{\text{H}}} [1 - \text{Erf}(z/\sqrt{2}H)], \quad (8)$$

where the obliquity parameter μ accounts for the increase in the obscuring column density due to the fact that the disk is illuminated obliquely (e.g. Neufeld & Maloney 1995; Herrnstein et al. 2005), $\text{Erf}(X)$ is the standard error function, and $n_{\text{H}}(r, z) = 2n_{\text{H}_2}(r, z)$ is the number of H nuclei. For the region where Thomson scattering becomes important and enhances X-ray obscuration (i.e. the Compton-thick regime; $N_{\text{H}}(r, z) \geq 1.5 \times 10^{24} \text{ cm}^{-2}$), we adopt the *effective* column density $N_{\text{H}}^{\text{eff}}(r, z) = \tau_{\text{T}} N_{\text{H}}$ for evaluating the attenuated X-ray heating rate, where the boosting factor is $\tau_{\text{T}} \sim 6.65 \times 10^{-25} N_{\text{H}}$ (Neufeld 2000).

Finally, in our calculation of $H_{\text{X}}/n_{\text{H}}$ with Equations 2 and 3, we assume that the X-rays that originate from the disk corona in the vicinity of the central BH were emit isotropically (Namekata & Umemura 2016) and the 1 – 100 keV X-rays account for $\sim 20\%$ of the bolometric flux (e.g. Neufeld et al. 1994; Netzer 2019), suggesting that $F_{\text{X}} = 0.2L_{\text{bol}}/4\pi r^2$. In addition to estimate the heating rate, we also compute the density distribution of the molecular gas with Equation 7 to find out the region where $n_{\text{H}_2}(r, z)$ fall in the favored range for maser excitation (i.e. $n_{\text{H}_2} = 10^7 - 10^{11} \text{ cm}^{-3}$). By comparing this region with the locations where the X-ray heating rate is sufficient to maintain $T_{\text{H}_2} \sim 400 - 1500 \text{ K}$, we identify the boundaries of the masing region within which the level population of water molecules could be inverted.

3.5 The Location and Outer Boundary of the Masing Region

Given that the predicted outer radii of the maser disks from the steady-state model cannot be reconciled with the observations for the majority of our sources, we focus our attention on the more general power-law disk model prescribed by Equation 5, with M_{D} and s treated as free parameters. In our analysis, we model every maser disk by choosing a set of (s, M_{D}) , with s varied between $-2.0 < s < 0.0$ in step of 0.1. For a given value of s , our model suggests that the outer radius of the masing region is an increasing function of M_{D} . By using the observed outer radius as the constraint, we try to fit the disk mass such that the predicted R_{out} can match with the observation.

In Column (3) of Table 2, we list the range of s in which we can find solutions for M_{D} , with Column (4), (5), & (6) indicating the best-fit M_{D} in unit of $10^4 M_{\odot}$ for three representative models with $s = -1.8$, $s = -1.4$, and $s = -1.0$, respectively. To compare the disk mass within the same reference radius, we also show in Column (7) the total disk mass \tilde{M}_{D} within $r = 1 \text{ pc}$ for each maser system with the assumption of $s = -1$ (Hure et al. 2011; Kuo et al. 2018a).

One can see that the disk masses within 1 pc are comparable for all maser systems, with the values falling within the narrow range of $\sim (1-10) \times 10^4 M_{\odot}$. In addition, the disk-to-BH-mass ratios $\tilde{M}_{\text{D}}/M_{\text{BH}}$ shown in Column (8) are all significantly smaller than unity, with a

mean value of $\tilde{M}_{\text{D}}/M_{\text{BH}} \sim 0.005$, consistent with the fact that most maser disks in our sample follow nearly perfect Keplerian rotation. Finally, we also note that the best-fit M_{D} are substantially smaller than the predictions from the steady-state accretion model, suggesting that the steady-state assumption is in question. Given $L_{\text{bol}} \sim 10^{44} \text{ ergs s}^{-1}$ and $M_{\text{BH}} \sim 10^7 M_{\odot}$ for most maser disks (see Table 2), Equation 6 predicts that \tilde{M}_{D} would be $\sim 1.0 \times 10^6 M_{\odot}$ if the accretion is in the steady state. This is $\sim 1 - 2$ orders of magnitudes greater than our best-fit M_{D} , suggesting that the the steady-state accretion disk is too massive to produce a small enough outer radius consistent with the observation.

To illustrate how the physical conditions of the gas define the boundaries of the masing region, we show in Figure 3 the X-ray heating rate and gas density distributions for each maser disk based on the $s = -1$ model. In each panel, the two vertical grey bars indicate the observed inner and outer radii of the maser disk. The green dotted and dot-dashed lines delineate the locations for the minimum and maximum density for maser excitation, respectively. The black solid line represent the points where the heating rate reaches $(H_{\text{X}}/n_{\text{H}})_{\text{max}}$ while the dashed line shows the curve for $(H_{\text{X}}/n_{\text{H}})_{\text{min}}$. It is expected that the gas lying beyond the maximum heating curve will become atomic, and the gas bound within the minimum heating curve will be too cold to mase. To produce luminous maser emissions, the gas needs to lie within the masing region marked by the blue shaded area, in which the gas density and temperature would fall in the favored ranges for population inversion.

It can be seen that the masing region typically lies close to the mid-plane of the disk except for NGC 1194, and the thickness of the masing region between R_{in} and R_{out} is typically $\sim 1 - 4H$. In addition, one can also infer that the X-ray heating rate per nucleus always increases with radius in every maser disk, suggesting that the gas temperature would increase with radius as well assuming T_{d} is roughly constant. As a result, we argue that the minimum temperature $T_{\text{min}} \sim 400 \text{ K}$ could not be the primary factor that determine R_{out} . As suggested by Figure 3, the outer radius of a maser disk can only be determined either by the maximum heating rate (e.g. NGC 4258, UGC 3789, etc.) or the minimum gas density n_{min} for maser pumping (e.g. NGC 2960, NGC 5765b, etc.), depending on the combination of L_{bol} , M_{BH} , and M_{D} . We will discuss this dependence in details in Section 4.3.

Finally, the readers should be aware that the outer radius of a maser disk predicted by our model should be seen as an approximation. In our simple modeling presented above, we ignore the effect of density perturbation of the molecular gas as a result of X-ray heating. Given the turbulence dominated disk in our analysis, we implicitly assume that the equilibrium density of the molecular gas after X-ray irradiation is comparable to the gas density before any injection of thermal energy. Taking the density perturbation into account would require a more rigorous modeling that involves solving the energy balance equation for the gas. This is beyond the scope of this paper, and we defer this to future work.

3.6 The Inner Edge and the Dust Sublimation Radius

One can see in Figure 3 that the density and heating rate requirements for efficient maser pumping does not impose a clear inner bound in the maser disk. This situation does not change no matter how we vary the model parameters, suggesting that the physical conditions of the gas alone may not be able to define the inner edge of a maser disk. Other factors might be involved.

Among the additional factors that could affect the production of water maser emissions, dust properties are the most important.

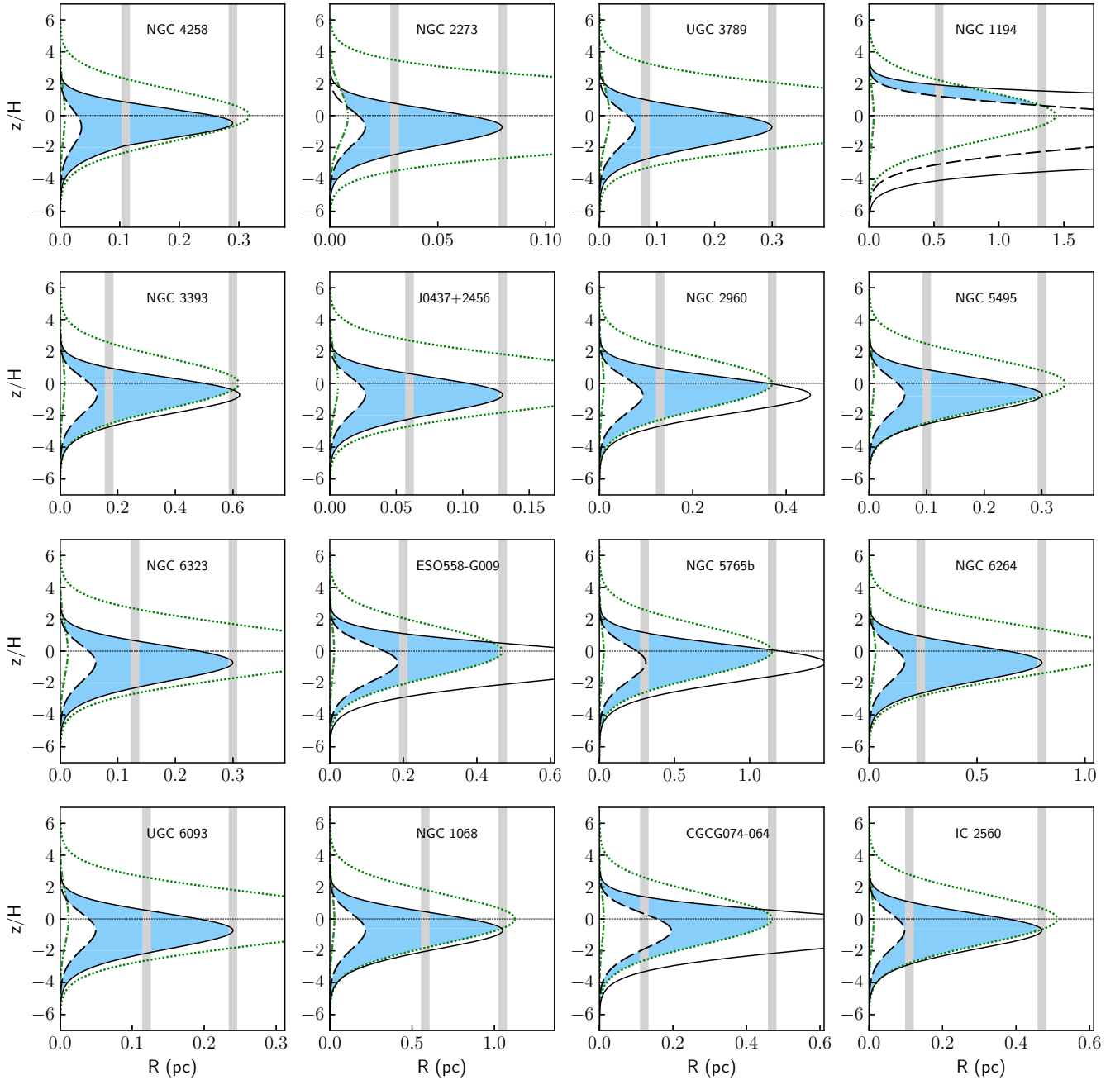


Figure 3. The distributions of the X-ray heating rate per hydrogen nucleus (H_X/n_H) and the number density of the molecular gas (n_{H_2}) for each of the H_2O megamaser disks in our sample. The horizontal axis gives the disk radius and the vertical axis designates the disk elevation normalized to the scale height H . The green dotted and dot-dashed lines indicate the locations in the disk where $n_{H_2} = 1 \times 10^7 \text{ cm}^{-3}$ and $1 \times 10^{11} \text{ cm}^{-3}$, the minimum and maximum density for population inversion, respectively. The black solid line represent the points where the heating rate reaches the critical value for molecular dissociation. The dashed line shows the curve of the minimum heating rate that ensures $T_{H_2} \gtrsim 400 \text{ K}$. The blue shaded area in each plot shows the region in which the gas density and temperature fall in the favored ranges for population inversion. The inner and outer radii of the maser disk are shown by the two vertical grey bars in each plot.

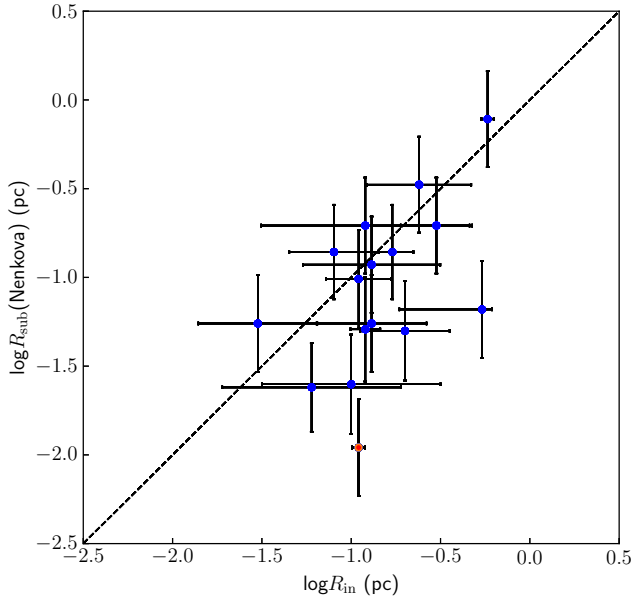


Figure 4. The comparison between the observed inner radius and the dust sublimation radius of the H₂O maser disks. The dashed line in the plot indicates the locations where $R_{\text{in}} = R_{\text{out}}$. Except for NGC 4258 marked by the filled red circle, R_{in} are comparable to R_{sub} for the majority of our maser disks given the measurement uncertainties.

As explained in Section 3.1, the presence of cold dusts is essential for maintaining population inversion by absorbing nonmasing far-infrared water lines trapped in the cloud. If the amount of dust particles are substantially reduced at some radius due to reasons such as dust sublimation, it is likely that the trapping of the far-infrared photons may become more significant, leading to an edge of the maser disk where the population inversion is quenched.

To explore this possibility, we estimate the dust sublimation radius for each maser disk (see Column (9) of Table 2) based on the prescription provided by [Nenkova et al. \(2008\)](#):

$$R_{\text{sub,Nenkova}} \approx 0.4 \left(\frac{L_{\text{bol}}}{10^{45} \text{ erg}^{-1}} \right)^{1/2} \left(\frac{1500 \text{ K}}{T_{\text{sub}}} \right)^{2.6} \text{ pc}. \quad (9)$$

In our calculation, we use L_{bol} from Table 2, with the assumption that dusts sublimate at the temperature $T_{\text{sub}} \sim 1500$ K. We estimate the uncertainty $\delta R_{\text{sub,Nenkova}}$ by adopting $\delta L_{\text{bol}} \sim 0.54$ dex, obtained from the comparison between L_{bol} estimated from X-ray spectroscopy and the [OIII] $\lambda 5007$ line for our sample ([Kuo et al. 2020a](#)). As noted in [Nenkova et al. \(2008\)](#), $R_{\text{sub,Nenkova}}$ is not a sharp boundary within which no dusts exist. Instead, it is an approximation that marks the radius across which the environment transitions from being dusty to dust-free as the individual components of the dust mixture gradually sublimate at different radii. It is expected that the largest grains can survive down to the innermost radius of the dusty torus probed by reverberation mapping observations (e.g. [Suganuma et al. 2006](#); [Kishimoto et al. 2007](#)), which is ~ 3 times smaller than $R_{\text{sub,Nenkova}}$.

In Figure 4, we compare the observed inner radius of the maser disk with the dust sublimation radius for all sources in our sample. This figure shows that the majority of the maser disks have their inner radii

consistent with $R_{\text{sub,Nenkova}}$ within $\sim 1\sigma$ ($\sim 75\%$) or $\sim 2\sigma$ ($\sim 19\%$) error. The only significant outlier in this comparison is NGC 4258 (the red square in the figure), for which R_{in} is considerably greater than $R_{\text{sub,Nenkova}}$ given the measurement uncertainties. This result suggests that, except for NGC 4258, dust sublimation may play a role in determining the inner radius of a maser disk. It is likely that dusts residing near the sublimation radius would become warmer and their efficiency as a heat sink ([Babkovskaia & Poutanen 2004](#)) for absorbing far-infrared photons gets reduced. In addition, the trapping of far-infrared photons by the masing clouds may become more significant as dusts gradually sublimate away at $R \sim R_{\text{sub,Nenkova}}$. This process may quickly destroy the population inversion, resulting in the observed inner edge of an H₂O maser disk.

4 DISCUSSION

4.1 The Characteristic Inner Radius

Our results from the last section suggest that the outer radius of a maser disk could be determined either by the minimum gas density or the maximum heating rate that enables efficient maser action. Moreover, the inner edge of the disk may result from the quench of population inversion near the dust sublimation radius. While the physical conditions of the gas and the dust appear to play an important role in defining the inner and outer boundaries of a maser disk, these conditions do not seem to directly explain why the inner radii of most maser disks are all around $R_{\text{in}} \sim 1.0 \times 10^5 R_{\text{S}}$ as shown in Section 2. In particular, if the inner edge of a maser disk is indeed constrained by the dust sublimation radius $R_{\text{sub,Nenkova}} \approx 0.4 (L_{\text{bol}}/10^{45} \text{ erg}^{-1})^{1/2}$, one would expect that R_{in} should depend more strongly on L_{bol} , rather than scale linearly with R_{S} , which is proportional to M_{BH} .

To explain the characteristic scale of $R_{\text{in}} \sim 1 \times 10^5 R_{\text{S}}$ in light of the dust sublimation radius, we find it helpful to replace L_{bol} in Equation 9 with $L_{\text{bol}} = \lambda_{\text{Edd}} L_{\text{Edd}}$, where λ_{Edd} is the Eddington ratio and $L_{\text{Edd}} = 1.26 \times 10^{38} (M_{\text{BH}}/M_{\odot})$ is the Eddington luminosity. This replacement allows one to express the dust sublimation radius in unit of R_{S} as

$$R_{\text{sub,Nenkova}} = 1.05 \times 10^5 \left(\frac{\lambda_{\text{Edd}}}{0.05} \right)^{1/2} \left(\frac{M_{\text{BH}}}{10^7 M_{\odot}} \right)^{-1/2} R_{\text{S}}. \quad (10)$$

The above equation directly implies that the dust sublimation radius in AGN in general does not equal $\sim 1.0 \times 10^5 R_{\text{S}}$ since its value depends substantially upon λ_{Edd} and M_{BH} . However, it is well-known that the BH masses for the Keplerian megamaser disks are typically $\sim 10^7 M_{\odot}$, likely resulting from the fact that disk megamasers are preferentially detected in local Seyfert 2 galaxies ([Kuo et al. 2011](#)) whose BH mass function peaks at $M_{\text{BH}} \approx 3 \times 10^7 M_{\odot}$ ([Heckman et al. 2004](#)). Moreover, the Eddington ratios of the majority of the Keplerian disk maser systems fall in the narrow range of $\lambda_{\text{Edd}} \sim 0.01 - 0.1$, with the median value ≈ 0.04 (see Table 5 and Figure 6 in [Kuo et al. 2020a](#)). Given that disk maser systems typically have $M_{\text{BH}} \approx 10^7 M_{\odot}$ and $\lambda_{\text{Edd}} \approx 0.04$, one can infer from Equation 10 that the dust sublimation radii of most Keplerian H₂O maser disks would be $\sim 1.0 \times 10^5 R_{\text{S}}$, the characteristic inner radius we see in Figure 1.

It is likely that this characteristic scale is deeply connected with the fine-tuning nature of the disk megamaser phenomenon and it reflects the dust sublimation radius of a gas disk in a certain phase of AGN evolution, with BH masses following the population for low redshift Seyfert 2 galaxies. As suggested in [Constantin \(2012\)](#), disk megamaser phenomenon may only occur in a certain (short) phase in the galaxy-AGN coevolution during which the mode of gas accretion

dramatically changes. We further speculate that Keplerian maser disks are more likely to arise in the phase in which the accretion disks are optically-thick, geometrically thin, with typical $\lambda_{\text{Edd}} \gtrsim 0.01$ (e.g. [Giustini & Proga 2016](#)). Given this speculation, the typical Eddington ratio distributions for local Seyfert galaxies (e.g. [Jones et al. 2016](#)) would imply that the disk megamasers with $\lambda_{\text{Edd}} \sim 0.01 - 0.1$ would outpopulate the ones with $\lambda_{\text{Edd}} \gtrsim 0.1$. It can be expected that if H_2O maser disks also exist at the centers of high redshift AGNs (e.g. quasars at $z > 2$), the Eddington ratio and BH mass distribution would be considerably different (i.e. $\lambda_{\text{Edd}} \gtrsim 0.1$ and $M_{\text{BH}} \gtrsim 10^9 M_{\text{BH}}$), leading to a distinctly different characteristic radius for high- z maser disks.

4.2 The Inner Radius of NGC 4258

As shown in Section 3.6, NGC 4258 is the most prominent outlier in our comparison between R_{out} and $R_{\text{sub,Nenkova}}$ for maser disks, suggesting that the inner edge of NGC 4258 requires explanations beyond the physical conditions of the gas and the dust in the disk. While one could resort to different mechanisms, such as the Bardeen-Peterson (BP) effect ([Caproni et al. 2007](#)), to explain its inner radius, we note that the present inner edge of NGC 4258 is partially defined by the observational constraints and it is the only source in our sample having this issue. Assuming a distance of 7.6 Mpc, the maser emissions from NGC 4258 terminate at an inner radius of $R_{\text{in}} = 0.11$ pc, corresponding to the position of the redshifted maser component whose radio LSR velocity is 1647 km s^{-1} . This maser feature lies quite close to the edge of the VLBI observing bands for NGC 4258 as reported in [Argon et al. \(2007\)](#), which provides the widest ever VLBI bandpass for NGC 4258, covering a velocity range between -706 km s^{-1} and 1676 km s^{-1} . The sensitive single-dish monitoring of NGC 4258 with the Green Bank Telescope (GBT) as part of the MCP also covers a similar velocity range, preventing one to explore masers beyond the current spectral limits. It would be interesting if future observations of NGC 4258 can cover a substantially wider spectral range and examine whether there are maser features lying well inside the present inner edge.

Aside from the observational constraints, we speculate that the inner edge of NGC 4258 could also be imposed by the significant inclination warp in this famous maser system. By comparing the orientations of all maser disks in our sample, it can be seen that while most maser disks are within $\sim 1^\circ - 2^\circ$ from being edge-on (e.g. [Kuo et al. 2011](#); [Gao et al. 2016](#); [Pesce et al. 2020a](#)), NGC 4258 displays the most significant inclination warp. Based on the disk modeling by [Humphreys et al. \(2013\)](#), the disk inclination at a radius $r \leq R_{\text{in}} = 0.11$ pc is $\leq 79.2^\circ$, showing that the deviation from the edge-on configuration would be greater than 20° if there are masers residing inside R_{in} . Given such large inclinations, it is possible that the effective coherent path length would reduce substantially, leading to weak maser emissions below the detection limit.

4.3 On the Detection of H_2O Gigamasers at High Redshifts

4.3.1 The Effect of Increasing Gain Length

Observations of the early universe have revealed strong evidence that galaxies or mergers once went through a extremely rapid and luminous phase of evolution, leading to intensive star formation and quasar activities that peaks at $z \sim 2 - 3$ ([Kotilainen et al. 2009](#); [Lapi et al. 2017](#)). During the most active phase of evolution, it is believed that a high fraction of luminous quasars may harbor $\gtrsim 10^9 M_\odot$ supermassive BHs at their cores (e.g. [Vestergaard & Osmer](#)

[2009](#); [Li et al. 2021](#)). As a result of immense energy injection into the surrounding gas, [Lo \(2005\)](#) speculates that AGN formation at the high- z galaxies could possibly trigger H_2O gigamasers, whose total maser luminosities could be $\gtrsim 10^3$ higher than those of low- z H_2O megamasers. If such gigamasers truly exist in the early universe, they could serve as a new class of high redshift distance indicators, providing an independent probe of the expansion rate of the early universe.

To access the possibility of discovering high- z H_2O gigamasers in disk configuration quantitatively, we estimate the flux densities of high- z maser disks based on the model presented in the last section. Our estimation suggests that the existing radio telescopes, such as the Very Large Array (VLA) and the GBT, would have sufficient sensitivities to detect these gigamaser disks if their typical radii can be $\gtrsim 20 - 30$ times greater than those of the low redshift maser systems (i.e. $R \sim 0.3 - 0.8$ pc).

As one can infer from [Lo \(2005\)](#), the flux density S_ν of a saturated maser source can be expressed as

$$S_\nu = (1+z) \frac{n_u \Delta P h\nu L_g^3}{D_L^2 \Delta\nu} \text{ erg s}^{-1} \text{ cm}^{-2} \text{ Hz}^{-1}, \quad (11)$$

where n_u is the density of H_2O molecules in the upper excited state, ΔP is the rate of maser transition from the upper to the lower state, $h\nu$ is the energy of a maser photon, L_g is the gain length for maser amplification, D_L is the luminosity distance to the source, and $\Delta\nu$ is the observing bandwidth at the observer's frame. The cubic dependence of L_g shown in the equation suggests that the maser flux density is highly sensitive to the gain length, which is expected to be comparable to the velocity coherent path length L_c in a maser disk.

Since maser action only take places when the gas density and temperature fall within the narrow ranges shown in Section 3.1, one could assume that on average $n_u \Delta P$ in the high- z environment would be comparable to that in local maser sources. Given this assumption, the key parameters that determine the maser flux density would be the the coherence path length L_c of the disk and the obvious inverse square dependence of distance D_L .

For the high-velocity maser components in a maser disk, the velocity coherent path length L_c at the tangent points at radius R is $L_c = 2(\delta V/V)^{1/2} R$, where δV and V are the gas velocity dispersion and the orbital velocity, respectively, suggesting that the gain length would increase linearly with R ([Lo 2005](#)). If the radius of a maser disk can increase by a factor of $\gtrsim 20 - 30$, the isotropic luminosity density of the source $L_\nu \equiv 4\pi D_L^2 S_\nu / (1+z)$ would increase by a factor of $\gtrsim 8000 - 27000$ due to the increase in L_c , making the source a H_2O gigamaser.

Assuming such H_2O gigamaser disks exist at $z \sim 2 - 3$, their luminosity distances would be $\sim 150 - 250$ times greater than a maser disk at the distance of ~ 100 Mpc assuming standard cosmology. The inverse square dependence of D_L would then lead to a decrease in the flux density by a factor of $\sim 20000 - 60000$. By considering the change in the flux density S_ν due to the factor $(1+z)$ and the increases in D_L and L_c based on Equation 11, one would expect that the flux densities of a 22 GHz H_2O gigamasers at $z \sim 2 - 3$ could be comparable to that of a local H_2O megamaser at ~ 100 Mpc. Given that the flux densities of known H_2O maser disks at $D_L \sim 100$ Mpc are typically $\sim 20 - 40$ mJy (e.g. [Kuo et al. 2013](#), [2015](#); [Gao et al. 2016](#)), the expected flux densities of the strongest maser features in a high- z gigamaser could range from a few mJy up to $\gtrsim 40$ mJy, suggesting that a few σ detections of the stongest lines are possible with a few hours of on-source integration time using the VLA, the GBT, and the High Sensitivity Array (HSA). Note that before applying the above estimation to high- z sources, one need to

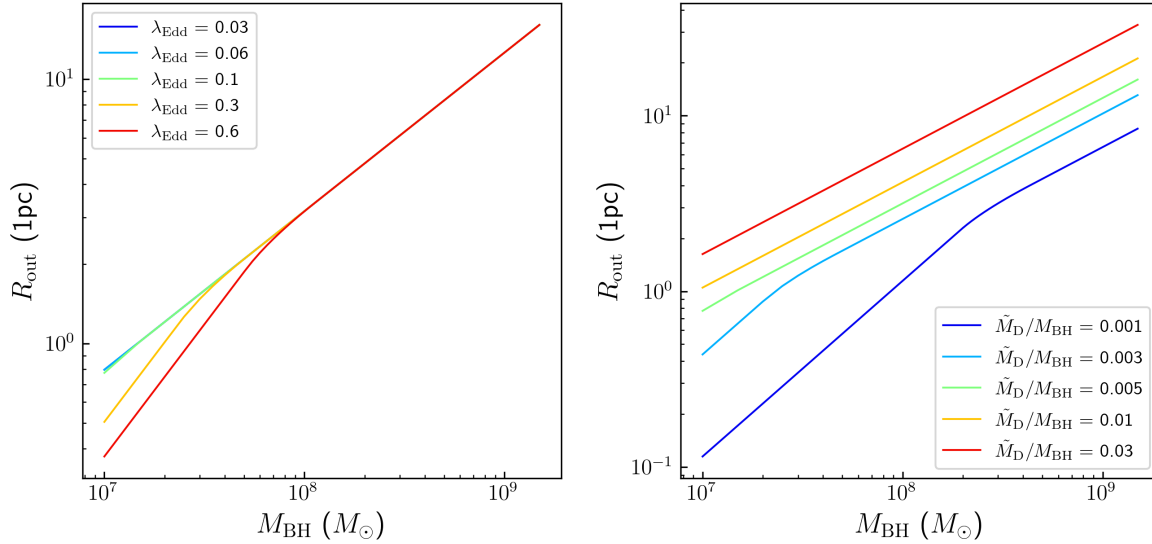


Figure 5. Left panel : the prediction of the outer radius of a megamaser disk with the BH mass ranging from $1.0 \times 10^7 M_{\text{BH}}$ to $1.5 \times 10^7 M_{\text{BH}}$, made with the assumption of $\tilde{M}_{\text{D}}/M_{\text{BH}} = 0.005$, where \tilde{M}_{D} is the disk mass within one pc. The blue, cyan, green, yellow, and red lines represent the predictions assuming the Eddington ratios of 0.03, 0.06, 0.1, 0.3, and 0.6 for the accreting BH, respectively; Right panel : The outer radius of a megamaser disk given the Eddington ratio of 0.1. The blue, cyan, green, yellow, and red lines indicate the predictions calculated based on $\tilde{M}_{\text{D}}/M_{\text{BH}} = 0.001, 0.003, 0.005, 0.01, 0.03$, respectively.

explore whether the high- z gigamaser disks could have significantly larger sizes than the ones in the local universe.

4.3.2 The Dependence of Maser Disk Size on the Black Hole Mass

Based on the observations of quasars in Vestergaard & Osmer (2009), it has been shown that the BH mass function of luminous quasars at redshifts between $1.5 \lesssim z \lesssim 3$ peaks at $M_{\text{BH}} \sim 1.5 \times 10^9 M_{\odot}$, and the Eddington ratios of these quasars tend to be $\lambda_{\text{Edd}} \gtrsim 0.1$. To see whether maser disks could exist around these $\gtrsim 10^9 M_{\odot}$ supermassive black holes, with their sizes significantly larger than the low redshift maser systems, we explore the dependence of maser disk size on black hole mass based on the disk model presented in Section 3.4. In this exploration, we adopt the disk profile $\Sigma(r) = \Sigma_{\text{out}}(r/r_{\text{out}})^{-1}$ with $c_{\text{g}} = 2 \text{ km s}^{-1}$ and fix the obliquity parameter at $\eta = 0.15$, a typical value for local H_2O maser disks. In addition, we set the bolometric luminosity in our model as $L_{\text{bol}} = \lambda_{\text{Edd}} L_{\text{Edd}}$, with λ_{Edd} varied between 0.03 to 0.6. Finally, we also assume that the ratio between the disk mass \tilde{M}_{D} within 1 pc and M_{BH} is comparable to those of the local maser disks (see Table 2) and set the ratio at five representative values ranging from 0.001 to 0.03. Given a combination of λ_{Edd} and $\tilde{M}_{\text{D}}/M_{\text{BH}}$, we model the heating rate and density distribution in the disk and calculate the outer radius of the masing region for BH mass between $1.0 \times 10^7 M_{\odot}$ and $1.5 \times 10^9 M_{\odot}$.

In the left panel of Figure 5, we show R_{out} as a function of M_{BH} for $\lambda_{\text{Edd}} = 0.03, 0.06, 0.1, 0.3$, and 0.6 , with $\tilde{M}_{\text{D}}/M_{\text{BH}} = 0.005$, the average disk-to-BH mass ratio for our sample. The right panel of Figure 5 shows the prediction of the outer radius for $\tilde{M}_{\text{D}}/M_{\text{BH}}$ ranging from 0.001 to 0.03 assuming $\lambda_{\text{Edd}} = 0.1$. It can be seen in both plots that the outer radius R_{out} for the cases with $\tilde{M}_{\text{D}}/M_{\text{BH}} \lesssim 0.005$ first increases with BH mass with a steeper slope, which drops distinctly when the BH mass is greater than a certain value (the critical BH

mass $M_{\text{BH}}^{\text{crit}}$ hereafter). It appears that $M_{\text{BH}}^{\text{crit}}$ varies depending on upon λ_{Edd} and $\tilde{M}_{\text{D}}/M_{\text{BH}}$.

To understand why the scaling between R_{out} and M_{BH} changes in different cases, we examine the heating rate and density distributions of the maser disks associated with different M_{BH} , λ_{Edd} , and \tilde{M}_{D} . We note that the outer boundary of the minimum density region lies beyond the maximum heating curve of the gas when $M_{\text{BH}} \ll M_{\text{BH}}^{\text{crit}}$. On the other hand, the edge of the minimum density region is bound within the maximum heating curve if $M_{\text{BH}} \gg M_{\text{BH}}^{\text{crit}}$. As a result, the outer radius of a maser disk is primarily determined either by the minimum density or the maximum X-ray heating, depending on whether the BH mass is greater or smaller than $M_{\text{BH}}^{\text{crit}}$.

Based on Equations (2) through (8), we find that the outer radius confined by the maximum heating can be expressed as

$$R_{\text{out}}^{\text{H}} = 0.77 \left(\frac{\lambda_{\text{Edd}}}{0.1} \right)^{-0.44} \left(\frac{\tilde{M}_{\text{D}}/M_{\text{BH}}}{0.005} \right)^{1.22} \left(\frac{M_{\text{BH}}}{10^7 M_{\odot}} \right) \text{ pc}, \quad (12)$$

, reminiscent of the scaling $R_{\text{out}} \propto M_{\text{BH}}$ found by Wardle & Yusef-Zadeh (2012). In the minimum density limited regime, the outer radius is related to the disk parameters as

$$R_{\text{out}}^{\text{D}} = 0.79 \left(\frac{\tilde{M}_{\text{D}}/M_{\text{BH}}}{0.005} \right)^{0.4} \left(\frac{M_{\text{BH}}}{10^7 M_{\odot}} \right)^{0.6} \text{ pc}, \quad (13)$$

consistent with the empirical relationship $R_{\text{out}} \propto M_{\text{BH}}^{0.57 \pm 0.16}$ found by Gao et al. (2017). For the disks in which $M_{\text{BH}} \approx M_{\text{BH}}^{\text{crit}}$, we find that $R_{\text{out}}^{\text{H}} \approx R_{\text{out}}^{\text{D}}$, suggesting

$$\frac{M_{\text{BH}}^{\text{crit}}}{10^7 M_{\odot}} \approx \left(\frac{\lambda_{\text{Edd}}}{0.1} \right)^{1.09} \left(\frac{\tilde{M}_{\text{D}}/M_{\text{BH}}}{0.005} \right)^{-2.04}. \quad (14)$$

The above equation indicates that the critical BH mass would be $\lesssim 10^8 M_{\odot}$ if $0.1 \lesssim \lambda_{\text{Edd}} \lesssim 1$ and $\tilde{M}_{\text{D}}/M_{\text{BH}} \gtrsim 0.005$, suggesting

that the outer radius of the maser disk around a $\gtrsim 10^9 M_\odot$ BH in a high- z quasar would be determined by $R_{\text{out}}^{\text{D}}$ if the gas disk is massive enough. As one can see in Figure 5, such high- z maser disks would have $R_{\text{out}} \sim 10 - 30$ pc given $\tilde{M}_{\text{D}}/M_{\text{BH}} \sim 0.005 - 0.03$, about $\sim 20 - 60$ times greater than the average outer radius of the local maser disks (i.e. $\bar{R}_{\text{out}} = 0.52$ pc). Based on the discussion in Section 4.3.1, we speculate that such large disk sizes could lead to H_2O gigamasers in high redshift galaxies.

Considering the typical angular-diameter distance D_A for a galaxy at $z \sim 2 - 3$ (i.e. $D_A \sim 1620 - 1760$ Mpc), the angular radius of a high- z maser disk with the physical size of $r \sim 10 - 30$ pc would be $\sim 1.2 - 3.8$ milliarcseconds, comparable to those of the local H_2O maser disks, suggesting that it is possible to apply the H_2O maser technique to high- z quasars with existing centimeter VLBI facilities. If one could further detect submillimeter water maser emissions (e.g. Pesce et al. 2016, 2023) from these high- z H_2O gigamaser disks, if exist, it is possible that future observations with the Event Horizon Telescope (EHT) would provide highly accurate maser imaging with $\sim 20 - 40$ microarcsecond resolution, leading to maser maps with fractional position uncertainties comparable to NGC 4258 (e.g. Argon et al. 2007; Humphreys et al. 2013).

5 DISCUSSION AND CONCLUSION

In this work, we examine whether the physical conditions favorable for population inversion of H_2O molecules can play the primary role for determining the inner and outer radii of an H_2O maser disk. In particular, we compare the observed radii of sixteen maser disks with the predictions from the steady-state accretion model and the power-law surface density model. We also apply our models to explore whether H_2O gigamaser disks could possibly exist in the high redshift universe. Our conclusions are summarized as follows :

1. The predictions from the well-known NM95 model that assumes steady-state accretion tend to over-predict the outer radii of the maser disks by a factor of $\sim 3 - 10$ for $\sim 75\%$ of our sample if one approximates the mass accretion rate as $\dot{M} \approx L_{\text{bol}}/\epsilon c^2$. In light of the results from our modeling, it is most likely that this discrepancy originates from the breakdown of the steady-state assumption for the majority of the maser disks.

2. The outer radii of all maser disks can be well explained if one adopts the disk model described by the power-law surface density profile. By examining the distributions of the X-ray heating rate and gas density in a X-ray illuminated molecular disk based on the power-law model, we are able to identify the masing region within which the physical conditions of the gas would enable efficient maser action. For all maser disks in our sample, we can find solutions that predict disk outer radii consistent with the observations. The best-fit models reveal that the masing regions tend to lie at the mid-plane of the disk, with the outer boundaries defined either by the maximum X-ray heating rate or minimum gas density for maser pumping, depending on the combination of M_{BH} , M_{D} , and λ_{Edd} .

3. The physical conditions of the gas alone cannot explain the inner radii of the maser disks. In the region well inside the inner radius of a maser disk, one can always find gas at a sufficiently high elevation having physical conditions suitable for maser excitation, suggesting that the inner edge of a maser disk involves physics beyond basic gas properties.

4. We find that the observed inner radii of the majority of the maser disks are roughly consistent with the dust sublimation radius $R_{\text{sub, Nenkova}}$ prescribed by Nenkova et al. (2008), which indicates the transition radius between dusty and dust-free environments. It is

likely that the trapping of far-infrared photons by the masing clouds becomes more significant as dusts gradually sublimate away at this transition region, leading the inner edge of a maser disk where the population inversion is mostly quenched.

5. Finally, our model predicts that H_2O gigamaser disks could exist around $\gtrsim 10^9 M_\odot$ supermassive BHs at the centers of high- z quasars. Their sizes could be as large as $\sim 10 - 30$ pc if the disk-to-BH-mass ratio is comparable or greater than the average value for local maser disks. The predicted flux densities of these systems range from a few mJy to $\gtrsim 20 - 30$ mJy, high enough to be detected with existing radio interferometers with a few hours of on-source integration. Future surveys of H_2O gigamasers from high- z quasars that could host these systems (e.g. Compton-thick AGNs; Kuo et al. 2020b) would provide a good test for our model.

ACKNOWLEDGEMENTS

We gratefully thank Dr. Fred Lo, the former director of National Radio Astronomy Observatory, for initiating the work for this paper before he passed away in 2016. This publication is supported by Ministry of Science and Technology, R.O.C. under the project 112-2112-M-110-003. This research has made use of NASA's Astrophysics Data System Bibliographic Services, and the NASA/IPAC Extragalactic Database (NED) which is operated by the Jet Propulsion Laboratory, California Institute of Technology, under contract with the National Aeronautics and Space Administration. In addition, this work also makes use of the cosmological calculator described in Wright (2006).

REFERENCES

- Argon A. L., Greenhill L. J., Reid M. J., Moran J. M., Humphreys E. M. L., 2007, *ApJ*, **659**, 1040
- Armitage P. J., 2022, *arXiv*,
- Babkova N., Poutanen J., 2004, *MNRAS*, **659**, 117
- Braatz J. A., Reid M. J., Humphreys E. M. L., Henkel C., Condon J. J., Lo K. Y., 2010, *ApJ*, **718**, 657
- Bregman Michal; Alexander T., 2009, *ApJ*, **700**, L192
- Bregman Michal; Alexander T., 2012, *ApJ*, **748**, 11
- Caproni A., Abraham Z., Livio M., Mosquera Cuesta H. J., 2007, *MNRAS*, **379**, 135
- Claussen M. J., Diamond P. J., Braatz J. A., Wilson A. S., Henkel C., 1998, *ApJ*, **500**, L129
- Collison A. J., Watson W. D., 1995, *ApJL*, **452**, L103
- Constantin A., 2012, *Journal of Physics: Conference Series*, **372**
- Desch S. J., Wallin B. K., Watson W. D., 1998, *ApJ*, **496**, 775
- Di Valentino E., et al., 2021, *CQGrA*, **38**, 110
- Fischera J., Dopita M. A., 2008, *ApJS*, **176**, 164
- Gammie C. F., Narayan R., Blandford R., 1999, *ApJ*, **516**, 177
- Gandhi P., Horst H., Smette A., Hönl S., Comastri A., Gilli R., Vignali C., Duschl W., 2009, *A&A*, **502**, 457
- Gao F., et al., 2016, *ApJ*, **817**, 17
- Gao F., et al., 2017, *ApJ*, **834**, 19
- Giustini M., Proga D., 2016, *MNRAS*, **456**, 374
- Gray M. D., Baudry A., Richards A. M. S., Humphreys E. M. L., Sobolev A. M., Yates J. A., 2016, *MNRAS*, **456**, 374
- Greene J. E., et al., 2016, *ApJL*, **826**, 6
- Greenhill L. J., Gwinn C. R., 1997, *Ap&SS*, **248**, 261
- Greenhill L. J., Gwinn C. R., Antonucci R., Barvainis R., 1996, *ApJL*, **472**, L21
- Greenhill L. J., et al., 2003, *ApJ*, **590**, 162
- Heckman T. M., Kauffmann G., Brinchmann J., Charlot S., Tremonti C., White S. D. M., 2004, *ApJ*, **613**, 109

- Herrnstein J. R., et al., 1999, *Nature*, 400, 539
- Herrnstein J. R., Moran J. M., Greenhill L. J., Trotter A. S., 2005, *ApJ*, 629, 719
- Humphreys E. M. L., Reid M. J., Greenhill L. J., Moran J. M., Argon A. L., 2008, *ApJ*, 672, 800
- Humphreys E. M. L., Reid M. J., Moran J. M., Greenhill L. J., Argon A. L., 2013, *ApJ*, 775
- Huré J. M., Hersant F., Surville C., Nakai N., Jacq T., 2011, *A&A*, 530
- Jones M. L., Hickox R. C., Black C. S., Hainline K. N., DiPompeo M. A., Goulding A. D., 2016, *ApJ*, 826
- Kartje J. F., Königl A., Elitzur M., 1999, *ApJ*, 513, 180
- King A. R., Pringle J. E., Livio M., 2007, *MNRAS*, 376, 1740
- King A. L., Davis T. M., Denney K. D., Vestergaard M., Watson D., 2014, *MNRAS*, 411, 3454
- Kishimoto M., Hönig S. F., Beckert T., Weigelt G., 2007, *A&A*, 476, 713
- Kormendy J., Ho L. C., 2013, *ARA&A*, 51, 511
- Kotilainen J. K., Falomo R., Decarli R., Treves A., Uslenghi M., Scarpa R., 2009, *ApJ*, 703, 1663
- Kotko I., Lasota J. P., 2012, *A&A*, 545
- Kuo C. Y., et al., 2011, *ApJ*, 727
- Kuo C. Y., Braatz J. A., Reid M. J., Lo K. Y., Condon J. J., Impellizzeri C. M. V., Henkel C., 2013, *ApJ*, 767
- Kuo C. Y., et al., 2015, *ApJ*, 800
- Kuo C. Y., Reid M. J., Braatz J. A., Gao F., Impellizzeri C. M. V., Chien W. T., 2018a, *ApJ*, 859
- Kuo C. Y., et al., 2018b, *ApJ*, 860
- Kuo C. Y., et al., 2020a, *MNRAS*, 498, 1609
- Kuo C. Y., et al., 2020b, *ApJ*, 892
- Lapi A., Mancuso C., Celotti A., Danese L., 2017, *ApJ*, 835
- Li W., Inayoshi K., Qiu Y., 2021, *ApJ*, 917
- Lo K. Y., 2005, *ARA&A*, 43, 625
- Lusso E., Piedipalumbo E., Risaliti G., Paolillo M., Bisogni S., Nardini E., Amati L., 2019, *A&A*, 628
- Maloney P. R., Hollenbach D. J., Tielens A. G. G. M., 1996, *ApJ*, 466
- Maoz E., McKee C. F., 1998, *ApJ*, 494
- Martin R., 2008, *MNRAS*, 387, 830
- Masini A., Celotti A., Campitiello S., 2022, *A&A*, 658
- Miyoshi M., Moran J., Herrnstein J., Greenhill L., Nakai N., Diamond P., Inoue M., 1995, *Nature*, 373, 127
- Namekata D., Umemura M., 2016, *MNRAS*, 460, 980
- Neškova M., Sirocky M. M., Nikutta R., Ivezić Z., Elitzur M., 2008, *ApJ*, 685, 160
- Netzer H., 2019, *MNRAS*, 488, 5185
- Neufeld D. A., 2000, *ApJ*, 542, L99
- Neufeld D. A., Maloney P. R., 1995, *ApJ*, 447
- Neufeld D. A., Maloney P. R., Conger S., 1994, *ApJ*, 628, L127
- Pesce D. W., Braatz J. A., Condon J. J., Gao F., Henkel C., Litzinger E., Lo K. Y., Reid M. J., 2015, *ApJ*, 810
- Pesce D. W., Braatz J. A., Impellizzeri C. M. V., 2016, *ApJ*, 827
- Pesce D. W., et al., 2020a, *ApJ*, 890
- Pesce D. W., et al., 2020b, *ApJL*, 891
- Pesce D. W., Braatz J. A., Henkel C., Humphreys E. M. L., Impellizzeri C. M. V., Kuo C.-Y., 2023, *ApJ*, 948
- Reid M. J., Braatz J. A., Condon J. J., Greenhill L. J., Henkel C., Lo K. Y., 2009, *ApJ*, 695, 287
- Reid M. J., Braatz J. A., Condon J. J., Lo K. Y., Kuo C. Y., Impellizzeri C. M. V., Henkel C., 2013, *ApJ*, 767
- Sawada-Satoh S., Kamenno S., Nakamura K., Namikawa D., Shibata K. M., Inoue M., 2008, *ApJ*, 680, 191
- Suganuma M., Yoshii Y., Kobayashi Y., 2006, *ApJ*, 639, 46
- Surcis G., Tarchi A., Castangia P., 2020, *A&A*, 637
- Vestergaard M., Osmer P. S., 2009, *ApJ*, 699, 800
- Wallin B. K., Watson W. D., 1997, *ApJ*, 476, 685
- Wallin B. K., Watson W. D., Wyld H. W., 1998, *ApJ*, 495, 774
- Wallin B. K., Watson W. D., Wyld H. W., 1999, *ApJ*, 517, 682
- Wardle M., Yusef-Zadeh F., 2012, *ApJL*, 750
- Wright E. L., 2006, *PASA*, 118, 1711